AN INVESTIGATION OF THE STARTUP TRANSIENT ELECTROKINETIC FLOW IN RECTANGULAR CHANNELS OF ARBITRARY DIMENSIONS, ZETA POTENTIAL DISTRIBUTION, AND TIME VARYING PRESSURE GRADIENT

By

ANDREW MICHAEL MILLER

A thesis submitted to the

Graduate School – New Brunswick

Rutgers, The State University of New Jersey

In partial fulfillment of the requirements

For the degree of

Master of Science

Graduate Program in Mechanical and Aerospace Engineering

Written under the direction of

Francisco Javier Diez-Garias

And approved by

_____

_____

_____

New Brunswick, New Jersey

January, 2017

ABSTRACT OF THE THESIS

An Investigation of the Startup Transient Electrokinetic Flow in Rectangular Channels of Arbitrary Dimensions, Zeta Potential Distribution, and Time Varying Pressure Gradient

By ANDREW MICHAEL MILLER

Thesis Director:

Francisco Javier Diez-Garias

The solution to the startup transient electroosmotic flow in an arbitrary rectangular micro-channel is derived analytically and validated experimentally. This full two dimensional transient solution describes the evolution of the flow through five distinct time periods until a final steady state condition is reached. The derived analytical velocity solution is validated experimentally for channels of different sizes and aspect ratios under time-varying pressure gradients. The experiments used a Time Resolved Micro Particle Image Velocimetry technique (TR-μPIV) to visualize and measure the startup transient velocity profiles. The results of this work captured the effects of time-varying pressure gradients across the microchannels and compared them to the results derived in the analytical solutions. This was accomplished by using small reservoirs at both ends of the channel, which allowed a time-varying pressure gradient to develop with a time scale on the order of the transient electroosmotic flow. Results showed that under these common conditions, the pressure build up between the reservoirs had a significant impact both on the transient startup of the electroosmotic flow and on the later temporal development of the velocity field in the channel. Finally, analytical solutions are provided to portray the fluid velocity development in microchannels with non-uniform zeta potentials. Experimental results validate the posed solution by visualizing the transient fluid velocity in microchannels fabricated with three PDMS and one quartz glass wall. These results show that the temporal development of the microchannel's velocity field is independent of the zeta potential distribution within the device.

Acknowledgements

I would like to extend my heartfelt and grateful acknowledgements to the various people that have gone so far out of their way to assist me in the completion of this work. First, I owe an enormous debt to my advisor, Professor Javier Diez, for guiding me through all the highs and lows that encapsulated my academic career. I started working with Professor Diez as an undergraduate researcher, while he himself was early in his career as an Assistant Professor. It was by his help and through his leadership that I was able to accomplish and grow so much, and it has been a true pleasure to see his career flourish as well. Your patience and eagerness to take on young researchers has had a deep and lasting impact on many of the students that have passed through your lab.

Alongside my advisor, I also extend my gratitude to all of my fellow coworkers and labmates from throughout the years. Arturo Villegas, Mehrnaz Youssefi, John Torres, Tom Reesbeck, Daniel Piwowar, Mena Tawfik, Mariusz Zarzecki, Ye Cheng, and Miquel Sureda. My time at Rutgers would not have been the same without your being there along the way. May you all prosper and find good fortune wherever you go.

A special thank you goes out to Professor Diez and Arturo Villegas, the coauthors of the paper this work is based on.

Finally, I thank my family for their patience and steadfast support. My mother and my sisters did so much to ground me, and I would not be here without them. Thank you for standing by me throughout it all.

Table of Contents

List of Illustrations

1 Introduction

Electrokinetics (EK) has become an important field of study for the design of microelectromechanical systems (MEMS), biomedical μTAS devices, and many other microfluidic apparatuses. Electroosmotic-driven flow is a fundamental electrokinetic phenomenon that has become one of the preferred methods to drive and control fluid flows in such devices. It is commonly used for particle manipulation at microscales. For instance, when colloidal systems are subjected to an applied electric field, a variety of different effects arise. These include the electrophoretic motion of charged particles relative to the liquid phase [1–2] and the electroosmotic fluid motion relative to a fixed surface-charged solid. These electrokinetic effects (both electroosmosis and electrophoresis) are often exploited in lab-on-chip devices providing advantages in terms of ease of operation, parallelization of analytical processes, highly resolved separations, and even mixing of analytes within microreactors.

Some authors have analyzed in great detail the characteristics of steady electrokinetically driven flows [3–13]. For instance, the steady electrokinetic flow in rectangular [3–4, 11] and circular [10] microchannels has been analyzed. Additionally, the effect of finite size reservoirs has been studied [7, 9] by considering the effect of an induced pressure gradient. Various experimental techniques have been applied to evaluate theoretical models of electroosmotic flows in microchannels. Yang and Yan [13] first used μPIV to investigate the flow development of borate buffer in a 300 μm square glass microchannel. This involved capturing images of the fluid flow at specific times after the electric field had been turned on. Different μPIV techniques have been applied [5–6, 8, 12] to calculate the steady electroosmotic velocity.

The transient electroosmotic flow has recently been studied in a range of electrokinetically driven devices [14–22]. Marcos et al. [14] investigated a frequency-dependent laminar electroosmotic flow in a closed-end rectangular microchannel. Shinohara et al. [15] developed a high-speed μPIV technique by combining a high-speed camera and a continuous wave (CW) laser. A similar μPIV technique [16–17] was used to investigate the transient development of the fluid flow in an electrokinetic closed cell. Researchers have also shown the development of a pressure gradient induced by the quasi-steady electrokinetic fluid flow's volumetric flow rate. Chang and Wang [18] accounted for a finite double layer thickness in circular and rectangular microchannels, showing the transient development periods. Chang and Wang [19] also described the theory for transient fluid flow in partially circular microchannels. In related work, the temporal development of electrokinetic fluid flow in channels less than 100 μm in width was first shown by Kuang et al. [20]. This was accomplished by using the laser induced photobleaching (LIFPA) technique. This same technique was employed to find the transient fluid development in a microchannel of only 10 μm in diameter [21]. Most recently, a technique [22] was proposed to find the transient development of particles' velocities in a microchannel by using time resolved μPIV (TR-μPIV). However, to date, the physics of the unsteady electrokinetic systems is still not fully understood, due to the lack of general solutions that can show all the transient effects.

The transient startup of EK systems is commonly characterized by a drastic increase in the fluid shear stresses, diffusion rates, and heat transfer rates throughout the system. In fact, such transient effects often result in a device performance that lies well outside the bounds of the normally observed the steady state operation. The fluid's transient

volumetric flow rate and the varying induced pressure gradient within a microdevice can greatly alter the system's operation, perhaps even damaging sensitive components. The impact of pressure variations within a device's electrokinetic startup regime have not been investigated yet. This paper proposes a theory to model the fluid behavior in arbitrary rectangular micro-channel and validates it experimentally.

This work derives an analytical expression for the transient electroosmotic flow in an arbitrary rectangular micro-channel. The proposed theoretical solutions are then validated by experiment. First, the full two dimensional velocity profile is analytically derived for different microchannel sizes and aspect ratios. This solution allows the identification of five distinct periods within the transient flow in a microchannel, which are then studied in detail for the geometries considered. Next, the time-varying pressure gradient induced by the volumetric flow rate is analyzed and compared between channels. Lastly, experimental measurements of the transient velocity field within rectangular microchannels of different dimensions and wall surface charge distributions are used to validate the analytical results.

2 Materials and methods

2.1 Analytical solution

The electroosmotic flow behavior in a microsystem can be generally described by two governing relations. The electrokinetic Navier-Stokes equations define the fluid's response to an applied electrical field and pressure gradient while the Poisson-Boltzmann relation gives the electrochemical response of the fluid to a surface charge at a boundary. The following study seeks to characterize the full transient response of a microfluidic system to any suddenly applied electrical field and developing pressure gradient. This study is applicable to any rectangular microchannel with an arbitrary zeta potential distribution at the walls. This analysis is constrained to systems with incompressible fluid flow and negligible heat generation and thermal effects. Reservoir effects will be included to account for a time varying volumetric flow rate and induced pressure gradient.

The Navier-Stokes equation for the electroosmotic flow can be expressed as:

$$\frac{\partial \bar{U}}{\partial t} + \bar{U} \cdot \nabla \bar{U} = -\frac{1}{\rho} \nabla p(t) + \nu \nabla^2 \bar{U} + \frac{\rho_e}{\rho} \bar{E}(t) \tag{1}$$

$$\nabla \cdot \bar{U} = 0 \tag{2}$$

$$\bar{U}(\bar{x}, 0) = 0 \qquad \bar{x} \in \Omega \tag{3}$$

$$\bar{U}(\bar{x}, t) = \bar{U}_{wall}(\bar{x}, t) \qquad \bar{x} \in \partial\Omega \tag{4}$$

where $\bar{U}$ is the flow velocity, $\bar{E}(t)$ is the applied electric field, $\nabla p(t)$ is the pressure gradient, $\bar{x}$ is the position vector, t is the time, ρ is the fluid density, μ is the viscosity, and ρ_e is the charge density. $\bar{U}_{wall}$ is a known function defining the Dirichlet boundary condition at the walls. Ω is the cross-section of a microfluidic channel. $\partial\Omega$ is the boundary of this domain.

The charge density is obtained from the Poisson-Boltzmann relation and the potential distribution ψ:

$$\nabla \cdot \left(\varepsilon_r \varepsilon_0 \nabla \psi \right) = -\rho_e \tag{5}$$

$$\rho_e = \sum_i z_i q n_i^0 e^{-\frac{z_i q \psi}{k_B T}} \tag{6}$$

where ε_0 is the permittivity of free space, ε_r is the relative permittivity of water, k_B is Boltzmann's constant, T is temperature, q is the elementary electrical charge, z_i is the number of valence charges on the molecule, n_i^0 is the concentration of the molecule in the free stream, and ψ is the induced electrostatic voltage in the fluid. Under the Debye-Hückel approximation ($\psi < (k_B T)/(z_i q)$), equations 5 and 6 can be linearized as:

$$\nabla^2 \psi = \frac{\psi}{\lambda^2} \tag{7}$$

$$\rho_e = -\frac{\varepsilon_r \varepsilon_0 \psi}{\lambda^2} \tag{8}$$

In cases where the Debye length (λ) is small compared to the dimensions of the channel, the effects of the electrokinetic double layer can be represented as a slip velocity at the boundary [23]:

$$\bar{U}_{wall}(\bar{x}, t) = -\frac{\varepsilon \varsigma_{wall}(\bar{x})}{\mu} \bar{E}(t) \qquad \bar{x} \in \partial\Omega \tag{9}$$

where ς_{wall} is the potential induced at the boundary between the stern layer and the diffuse layer by the surface charge of the wall. Since the Debye length is small compared to the dimensions of the channel and the temperature and concentration gradients are both zero in the bulk of the fluid, the electrokinetic double layer of the channel's walls does not fluctuate along the length of the channel. Additionally, the slip velocity at any point on the

boundary will depend on neither the gradient of the zeta potential along the channel wall nor on the zeta potential distribution of another portion of the wall in the channel.

For a symmetric electrolyte, the time scale to establish the Smoluchowski velocity within the Debye layer is estimated from Minor et al. [24] as $\tau_{dl} = O(\lambda^2/D)s \sim 10^{-12}\,s$, where *D* is the ion diffusion coefficient. The time scales for electrophoretic and electroosmotic velocities can be estimated [24] as $\tau_{ep} = O(10^{-7})s$ and $\tau_{eof} = O(10^{-3})s$ respectively. Therefore, the electrokinetic startup of the fluid's double layer can be taken as instantaneous compared to the fluid transient velocity due to differences in time scales $\tau_{dl} << \tau_{ep} \sim \tau_{eof}$.

An initial electric field and a pressure gradient applied across the channel induce fluid flow between the finite reservoirs. The relative fluid volume in each reservoir changes in proportion to the volumetric flow rate. For two reservoirs with the same constant cross-sectional area, the induced pressure gradient can be written as a function of time and the volumetric flow rate:

$$\frac{1}{\rho}\nabla p(t) = \frac{1}{\rho}\nabla p_0 + 2\frac{g}{L_{Ch}A_{resv}}\int_0^t Q(\tau)\,d\tau \tag{10}$$

$$Q(t) = \iint_{\Omega}\left(\bar{U}\cdot\hat{n}\right)dA \tag{11}$$

where *Q* is the volumetric flow rate, $\hat{n}$ is the unit vector parallel to the axis of the channel, L_{Ch} is the length of the channel, *g* is gravity, and A_{resv} is the cross-sectional area of the reservoirs. ∇p_0 is the initial pressure gradient in the system. With the time varying pressure gradient expressed in this manner and with ρ_e taken to be zero everywhere in the domain except for the boundaries, Eq. (1) can be written as an integral-differential equation:

$$\frac{\partial \bar{U}}{\partial t} + \bar{U}\cdot\nabla\bar{U} = -\frac{1}{\rho}\nabla p_0 + \nu\nabla^2\bar{U} - 2\frac{g}{L_{Ch}A_{resv}}\int_0^t\iint_{\Omega}\left(\bar{U}\cdot\hat{n}\right)dA\,d\tau \tag{12}$$

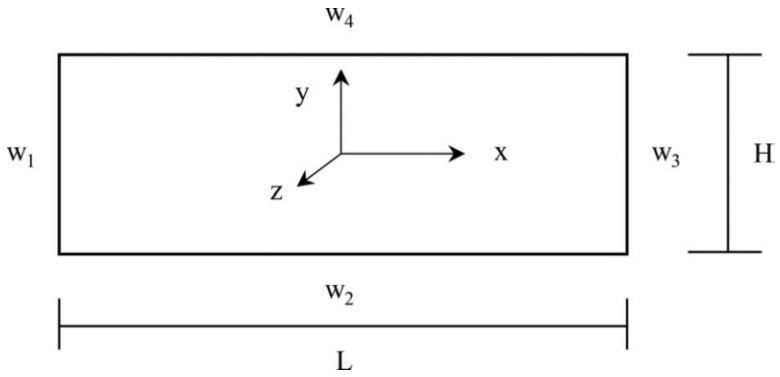

Figure 1. Cross section of the microfluidic channel with the electric field and pressure gradient acting in the z-direction. The fluid velocity also is aligned with the z-direction. The boundaries are numbered for convenience.

The domain Ω is constrained to a rectangle of width L and height H, as shown in Fig. 1. The origin of the coordinates system is located at the center of the channel and the z-axis is orthogonal to the channel's cross-section. The geometry does not change in the z-direction. The boundaries of the rectangular domain are numbered (1-4) for convenience in the following discussion.

The flow is considered fully developed inside the channel and the electric field lines are considered parallel to the z-direction. This simplifies Eq. (12) to a single equation with a given set of boundary conditions and an initial condition:

$$\frac{\partial w}{\partial t} = -\frac{1}{\rho}\frac{dp}{dz}\bigg|_o + \nu\left(\frac{\partial^2 w}{\partial x^2} + \frac{\partial^2 w}{\partial y^2}\right) - 2\frac{g}{L_{Ch}A_{resv}}\int_0^t \int_{-H/2}^{H/2}\int_{-L/2}^{L/2} w\,dx\,dy\,d\tau \tag{13}$$

$$w_{slip,\,i}(\bar{x},t) = -\frac{\varepsilon\varsigma_i(\bar{x})}{\mu}\bar{E}(t) \qquad \begin{matrix}\bar{x}\in\partial\Omega \\ i=1,2,3,4\end{matrix} \tag{14}$$

where $\varsigma_i(\bar{x})$ refers to the zeta potential distribution along the i^{th} channel wall, i ranges from 1 to 4. $w_{slip,i}$ is the slip velocity along the i^{th} wall. The initial condition is $w(x,y,0)=0$ everywhere except at the boundaries where the slip condition applies.

A solution to this transient electrokinetic flow field relevant to many realistic scenarios encountered in the lab and in industry will be presented next. It will be demonstrated from the analytic solution that the time scales associated with the startup of the electroosmotic flow field are independent of the zeta potential distribution in the channel. This will be validated by experiment later in this work.

2.1.1 Special Cases

Many microdevices encountered in lab or industrial use are fabricated by a select set of methods. In some cases, every wall of the microchannel is composed of borosilicate or quartz glass. In other cases, the microfluidic device is fabricated from casting PDMS in a mold. This PDMS is then bonded to either a sheet of glass, or it is bonded to another layer of PDMS. For each of the listed cases, each wall that is comprised of the same material exhibits the same zeta potential. Since the top of the channel and the side walls consist of the same material:

$$\varsigma_1 = \varsigma_3 = \varsigma_4 \tag{15}$$

The bottom of the channel, ς_2, can be either equal to the zeta potentials of the other boundaries or independent, as in the case of PDMS bonded to glass. Therefore, the boundary conditions for this problem can be written as:

$$w\left(x, -\frac{H}{2}, t\right) = -\frac{\varepsilon\varsigma_2}{\mu} E(t) \tag{16}$$

$$w\left(-\frac{L}{2}, y, t\right) = w\left(\frac{L}{2}, y, t\right) = w\left(x, \frac{H}{2}, t\right) = -\frac{\varepsilon\varsigma_1}{\mu} E(t) \tag{17}$$

The solution to Eq. (13) is then found by using the method of separation of variables (Appendix A). The velocity at every point and time of the cross section can be expressed as:

$$w(x,y,t)=-\frac{\varepsilon E\zeta_1}{\mu}+\frac{\varepsilon E}{\mu}\left(\zeta_1-\zeta_2\right)\frac{2}{\pi}\sum_{k=1}^{\infty}\frac{1+\left(-1\right)^{k+1}}{k}\sin\left(\frac{k\pi\left(x+\frac{L}{2}\right)}{L}\right)\frac{\sinh\left(\frac{k\pi\left(-y+\frac{H}{2}\right)}{L}\right)}{\sinh\left(\frac{k\pi H}{L}\right)}$$
$$-\frac{2H^2}{\pi^3\mu}\frac{dp}{dz}\sum_{j=1}^{\infty}\frac{1+\left(-1\right)^{j+1}}{j^3}\left[1-\frac{\cosh\left(\frac{j\pi x}{H}\right)}{\cosh\left(\frac{j\pi L}{2H}\right)}\right]\sin\left(\frac{j\pi\left(y+\frac{H}{2}\right)}{H}\right)$$
$$+\sum_{n=1}^{\infty}\sum_{m=1}^{\infty}\left\{\left[\frac{4\varepsilon E\zeta_1}{mn\mu\pi^2}\left(1+\left(-1\right)^{n+1}\right)\left(1+\left(-1\right)^{m+1}\right)-\frac{4\varepsilon E\left(\zeta_1-\zeta_2\right)}{H^2\mu}\frac{m}{n}\left[\frac{1+\left(-1\right)^{n+1}}{\frac{n^2\pi^2}{L^2}+\frac{m^2\pi^2}{H^2}}\right]\right.\right.$$
$$\left.+\frac{4H^2}{\pi^4\mu}\frac{dp}{dz}\frac{\left(1+\left(-1\right)^{m+1}\right)}{m^3}\left[1-\frac{\frac{n^2\pi^2}{L^2}}{\left(\frac{m^2\pi^2}{H^2}+\frac{n^2\pi^2}{L^2}\right)}\right]\frac{\left(1+\left(-1\right)^{n+1}\right)}{n}\right]$$
$$\left.\times\sin\left(\frac{n\pi\left(x+\frac{L}{2}\right)}{L}\right)\sin\left(\frac{m\pi\left(y+\frac{H}{2}\right)}{H}\right)e^{-\nu\pi^2\left(\frac{n^2}{L^2}+\frac{m^2}{H^2}\right)t}\right\}$$

(18)

The transient volumetric flow rate is then found by integrating the flow velocity profile across the microchannel's cross-section (Eq. (11)). Knowledge of the volumetric flow rate is important to understanding how a microfluidic system will perform and to improve the design of such a system. Many microfluidic systems are designed to deliver exact amounts of fluid to various sensors and locations as well as to specifically regulate the fluid transport throughout the device. Knowledge of the transient volumetric flow rate will increase the accuracy of such devices.

The pressure gradient a microchannel can generate is also vital to the performance of many devices. The transient pressure gradient across a microchannel can be calculated

from Eq. (10). The steady state maximum pressure gradient that can be developed is found when the volumetric flow rate is zero. At this point, the averaged cross-sectional electroosmotic velocity and the average velocity induced by the pressure gradient are equal to and opposite each other. When such a condition is met within a microchannel, the fluidic behavior is entirely dependent on the hydrodynamic and electrokinetic properties of the channel and is independent of the fluidic system's reservoirs. This is commonly the case for a closed cell, in which an electric field is used to drive fluid into a sealed reservoir. This condition might also arise in more complicated microfluidic devices where gates can keep channels sealed while an electric field is applied.

Regardless of whether the zeta potential is the same for all the walls in the microchannel, or whether the zeta potential distribution is asymmetric, the temporal term in the microchannel's velocity field is unchanged (Eq. (18)). This can be extended to show that the time constants pertaining to the transient development of the electroosmotic flow in any microdevice are functions only of the viscosity of the fluid and the geometry of the channel.

2.2 Experimental method

2.2.1 Electrophoretic and electroosmotic velocities

To validate the theory and numerical results, a time-resolved micro particle image velocimetry (TR-μPIV) technique is used to obtain the experimental transient electroosmotic flow velocity. Fluorescent microspheres are used as tracer particles. The velocity of the particle at every time and position of the cross-section area can be expressed as:

$$w_{PIV} = w_{ep} + w_{eof} + w_{pres} \tag{19}$$

where w_{PIV} is the velocity of the particle measured from the PIV system, w_{ep} is the electrophoretic velocity of the tracer particle, w_{eof} is the electroosmotic flow velocity, and w_{pres} is the velocity induced by the adverse pressure gradient. The time scale differences between electrophoretic $\tau_{ep} = O(10^{-7})s$ and electroosmotic velocities $\tau_{eof} = O(10^{-3})s$ [22, 24] allow calculating w_{ep} and w_{eof} simultaneously when the induced velocity created by the pressure gradient is negligible. However, if the pressure gradient evolves rapidly within the startup transient electroosmotic flow, the electroosmotic velocity field is unable to fully develop before being affected by the velocity induced by the adverse pressure gradient. This effect is shown in the results section for channels larger than 800 μm per side, where the fluid velocity in the center of the channel does not reach a steady electroosmotic velocity. Consequently, the experimental unsteady flow velocity in the channel can be written as:

$$w = w_{eof} + w_{pres} = w_{PIV} - w_{ep} \tag{20}$$

To calculate the electrophoretic velocity of the tracer particles, a high speed camera is needed to capture the movement of the particles at the center of the channel while the flow is still at rest ($w=0$). During this period of the transient development, the electrophoretic velocity is equal to the measured velocity ($w_{PIV}=w_{ep}$). Since the electrophoretic velocity becomes independent of time after it is fully developed, the flow velocity can be calculated thereafter by Eq. (20).

To understand the influence of the induced pressure driven velocity profile, and to verify if the flow has reached a steady state electroosmotic flow velocity, the electroosmotic velocity can be approximated by the linear Helmholtz-Smoluchowski equation for rectangular channels that do not present an overlapped EDL. In this case, the steady state electroosmotic flow velocity in the cross section of the rectangular channel is obtained by solving the Poisson equation with a zero pressure gradient:

$$\left(\frac{\partial^2 w_{ss,eof}}{\partial x^2}+\frac{\partial^2 w_{ss,eof}}{\partial y^2}\right)=0 \tag{21}$$

where the boundary conditions are obtained from Eqs. (16) and (17) for a channel composed of two different materials. The analytical solution is obtained by separation of variables [6] and used as a reference in the result section. It can be written as:

$$w_{ss,eof}=-\frac{\varepsilon E}{\mu}\zeta_1+\frac{\varepsilon E}{\mu}(\zeta_1-\zeta_2)\frac{2}{\pi}\sum_{k=1}^{\infty}\frac{1+(-1)^{k+1}}{k}\sin\left(\frac{k\pi\left(x+\frac{L}{2}\right)}{L}\right)\frac{\sinh\left(\frac{k\pi\left(-y+\frac{H}{2}\right)}{L}\right)}{\sinh\left(\frac{k\pi H}{L}\right)} \tag{22}$$

After the steady state velocity profile has been reached, the effect of the induced pressure gradient driven velocity profile can be obtained by using the Navier-Stokes equations for zero slip velocity at the walls:

$$0 = -\frac{1}{\rho}\nabla p(t) + \nu\nabla^2\bar{U} \tag{23}$$

The analytical solution is obtained by separation of variables [6] and it can be written as:

$$w_{pres} = -\frac{2H^2}{\pi^3\mu}\frac{dp}{dz}\sum_{j=1}^{\infty}\frac{1+(-1)^{j+1}}{j^3}\left[1-\frac{\cosh\left(\frac{j\pi x}{H}\right)}{\cosh\left(\frac{j\pi L}{2H}\right)}\right]\sin\left(\frac{j\pi\left(y+\frac{H}{2}\right)}{H}\right) \tag{24}$$

The evolution of the flow rate can then be obtained from $Q = Q_{ss,eof} + Q_{pres}$. The flow rate per cross-sectional area due to the steady state electroosmotic velocity for zero pressure gradient can be expressed as the average cross-sectional electroosmotic velocity:

$$\frac{Q_{ss,eof}}{HL} = -\frac{\varepsilon E}{\mu}\zeta_1 + \frac{\varepsilon E}{\mu}(\zeta_1-\zeta_2)\frac{2}{\pi^3}\frac{L}{H}\sum_{k=1}^{\infty}\frac{1+(-1)^{k+1}}{k^3}\frac{\cosh\left(\frac{k\pi H}{L}\right)-1}{\sinh\left(\frac{k\pi H}{L}\right)} \tag{25}$$

The evolution of the flow rate per cross-sectional area due to the adverse pressure gradient can be expressed as the average cross-sectional pressure induced velocity:

$$\frac{-Q_{pres}}{HL} = \frac{H^2}{12\mu}\frac{dp}{dz}\left[1-\frac{6H}{L}\sum_{j=1}^{\infty}\frac{2}{\pi(2j-1)}\tanh\left(\frac{\pi(2j-1)}{2}\frac{L}{H}\right)\right] \tag{26}$$

The minus sign refers to the negative induced flow rate due to the pressure gradient. After the electroosmotic steady state is reached, the evolution of the flow rate is dependent only on the pressure gradient differences due to the finite size of the reservoirs.

2.2.2 Experimental setup

To further validate the theory, a TR-μPIV system is used to measure the transient velocity. The conceptual layout of the system is sketched in Fig. 2. A picture of the experimental setup is provided in Fig. 3.

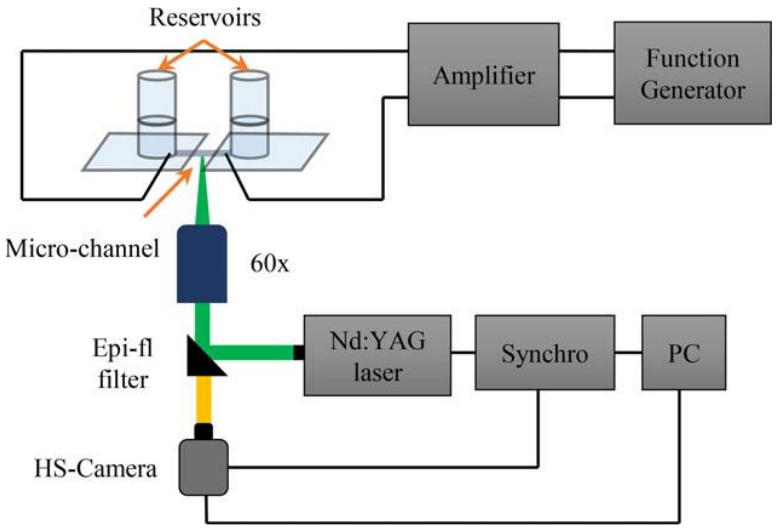

Figure 2. Conceptual sketch of the TR-μPIV system used to measure the instantaneous velocities of the tracer particles.

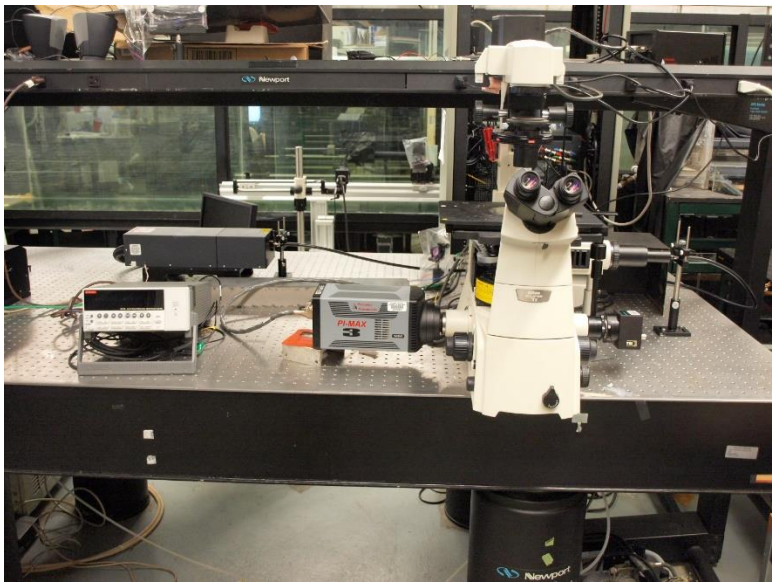

Figure 3. A picture of the experimental setup used throughout this set of experiments.

The experimental setup is comprised of an epi-fluorescence microscope (Model ECLIPSE E600FN, Nikon) with a 40x (*NA* = 0.75) objective lens and a 2 Gb Photron Ultima APX-RS high-speed digital camera (10-bit CMOS sensor, 1024 × 1024 pixel with 17.5 μm^2 pixel size) capable of 3000 fps at the maximum resolution. The light source is a pulsed high-speed Nd-YAG laser (Pegasus, New Wave Research). The light passes through an optical filter cube with a dichroic mirror to reach the microfluidic device. The fluorescent tracer particles suspended in the working solution are excited by the light, and the emitted fluorescent light is captured by the high-speed camera. Several image planes are taken within the height of the channel to capture the full velocity field in the cross section of the channel. The obtained PIV images are cross-correlated using INSIGHT 3G PIV software (TSI) to find the instantaneous velocity vector fields. To ensure that the voltage drop from the high-voltage power supply (model SL2KW by Spellman) is applied instantaneously, a high-speed switch circuit was built to act as a gate between the power supply and the microdevice. The high speed power supply switch has the capability of ramping to full voltage and current within 1.2 μs of receiving a trigger pulse. This pulse is supplied by the camera to ensure proper synchronization.

Fluorescent polystyrene particles of 1 μm diameter (Thermo Scientific FLUORO-MAX R900) are used as tracer particles. These particles are added to the buffer solution in an amount of 1×10^{-3} mg/mL. The peak values for the absorption and emission fluorescent wavelengths are 542 nm and 612 nm, respectively, with a density of 1.05 g/cm^3 and an index of refraction of 1.59 (589 nm, 25º C). These properties, in combination with a 40x objective (NA = 0.75), result in a depth of field during the measurements of 5.3 μm [12]. The particles' surfaces are treated with carboxyl groups (−COOH), which become

negatively charged ($-COOH^-$) when suspended in most aqueous solutions. The particles are suspended in a 100 mM borate buffer solution (pH 8.7), which is the working fluid used throughout these experiments.

The experiments were conducted at the center of five different sizes of rectangular glass channels, each with a length of 50 mm. Three of the glass channels were square in cross-section, measuring 300, 500, and 800 μm per side. The other two glass channels were rectangular in cross-section, measuring 500×5000 μm and 800×8000 μm in size. Each channel was operated with an applied electric field of 100 V/cm. Additionally, two PDMS/glass channels with cross-sectional dimensions of 360×1000 μm and 460×1000 μm were tested with an applied electric field of 200 V/cm and a channel length of 15 mm.

Since the borate buffer solution is 100 mM, the Debye length is $\lambda=9.6\times10^{-10}$ m. This gives a ratio between Debye length and channel width on the order of $\lambda/H \sim 10^{-6}$. Therefor the effects of the electrokinetic double layer can be represented as a slip velocity at the boundary of the channel.

3 Results

3.1 Analytical results

The solution for the transient electroosmotic flow derived analytically in Sec. 2.1 will be presented graphically and validated by experiment for microchannels of different sizes, aspect ratios, and zeta potentials. The analytical solution for the transient velocity profile allows the identification of five distinct periods within the transient flow in a microchannel.

In Period 1, the electroosmotic flow, EOF, is initiated as a slip velocity at the channel's walls induced by an instantly applied electric field. Period 1 is characterized by the slip velocity along each wall diffusing towards the center of the channel. As such, the fluid at the center of the microchannel is approximately at rest throughout this phase and is not accelerated until Period 1 has ended.

Fluid velocity measurements taken at the center of a microchannel during Period 1, away from the walls, would therefore not see the EOF. For instance, particle velocity measurements taken at the center of a microchannel during Period 1 would show a constant velocity due only to electrophoresis. For most microchannels encountered in normal lab and industrial use, the duration of Period 1 is short (typically t < 5-10 ms). A more general approximation of the time constant associated with the end of Period 1 is $\tau_1 = O(d^2/(20 * \upsilon))$, where d is the shortest cross-sectional dimension of the microchannel (either the channel's height or width), and υ is the kinematic viscosity of the fluid. This time constant approximates when the electrokinetically induced slip velocity of the channel's walls has diffused into the center of the channel, accelerating the fluid at the center of the channel to 10% of it its fully developed EOF velocity.

In Period 2, the electrokinetically induced velocity at the walls has diffused into the center of the channel, and the fluid across the entire channel is now accelerating towards a fully developed EOF velocity profile. Particle measurements performed during this phase in the center of the channel will visualize this acceleration as they transition from being only affected by the electrophoretic velocity to being affected by the combined electrophoretic velocity and the developing EOF velocity. Similar to Period 1, the length of Period 2 is typically short for most microchannels encountered in the lab and in industry (5-10 ms < t < 20-100 ms). As a general approximation, the time constant associated with the end of Period 2 is typically ten times longer than the time constant associated with the end of Period 1. $\tau_2 = O(10 * \tau_1)$.

Period 3 of the microchannel's transient development is characterized by a quasi-steady state flow field due to a constant and fully developed EOF. Particle measurements collected anywhere in the channel during this phase will show a steady velocity resulting from the steady and fully developed EOF and electrophoretic velocities. The beginning of Period 3 is typically when t > 20-100 ms. Period 3 is also most crucially characterized by the absence of a pressure gradient (or negligible pressure gradient) across the channel. When operating the microchannel with finite reservoirs at each end, a pressure differential builds up as fluid is pumped from the inlet reservoir to the outlet reservoir. At some point, depending on the channel's volumetric flow rate and reservoir sizes, the induced pressure gradient will give rise to a flow similar in magnitude and opposite in direction to the fully developed EOF velocity field characterizing Period 3. The result is that the measured flow field is not only affected by the EOF but also by a time-varying pressure gradient. The

beginning of this phenomena marks the end of Period 3 and the beginning of Period 4 in the microchannel's transient development.

Period 4 of the microchannel's transient development is characterized by the induced pressure gradient across the channel growing in strength as more fluid is pumped between the inlet and outlet reservoirs. As this occurs, an adverse velocity field induced by the pressure gradient is becoming stronger and counteracting the steady EOF velocity in the channel. This in turn decelerates the volumetric flow rate within the microchannel, driving the rate at which fluid is being pumped from the inlet reservoir to the outlet reservoir closer and closer to zero. Throughout Period 4, any measurements made of the particles' velocities will be affected by the electrophoretic velocity, the EOF, and a time-varying pressure gradient.

The end of Period 4 and the start of Period 5 is marked when the volumetric flow rate within the channel has reached zero. This signifies that rate at which the fluid is being pumped by the induced electric field has been completely counteracted by the adverse flow rate induced from the pressure gradient developed between the reservoirs. Period 5 is the final steady state condition for the microchannel's flow field.

The flow profile exhibited in Period 5 is the same as is developed in a closed electroosmotic cell microdevice. In such a device, fluid moves in one direction along the walls due to the electroosmotic effect, while simultaneously flowing in the opposite direction along the center of the channel in order to balance the pressure build up in the sealed reservoir. This steady state condition results in a zero net volumetric flow rate and a negative fluid velocity along the center of the channel (opposite the direction of the EOF).

Some variants of the five periods occur depending on the size and aspect ratio of the channel and they will be explained next.

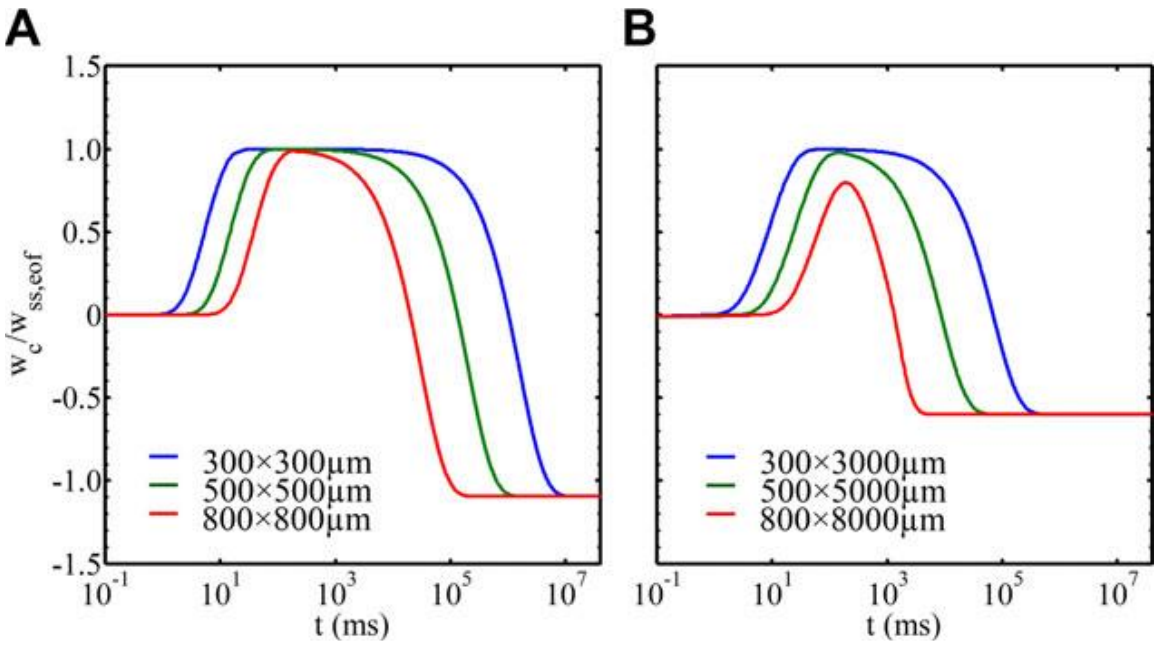

Figure 4. The temporal evolution of the analytical velocity at the center of the glass channels (wc) under an applied electric field of 100 V/cm for both (A) square and (B) rectangular channels.

The five periods previously described can be observed when plotting the transient flow velocity along the center of the channel as a function of time, as shown in Fig. 4. This figure illustrates the results from Eq. (18) for three different sizes of square microchannels, as well as for three higher aspect ratio rectangular channels. The depicted velocity profiles show a well define Period 1 ($t < 5$-10 ms) where the flow velocity in the center of the channel is zero, followed by a Period 2 (5-10 ms $< t <$ 20-100 ms) where the flow velocity increases rapidly. Next, in Period 3 (20-100 ms $< t <$ 200-1×10^4 ms), the EOF portion of the flow profile has reached steady and fully developed conditions, as shown by the constant velocities. In Period 4, which has a starting time that varies significantly

depending on the channel dimensions (i.e.: 200-1×10^4 ms < t < 1×10^4-1×10^7 ms for the geometries considered here), the velocity quickly decreases due to the developing adverse pressure gradient between the reservoirs. In Period 5, the velocity in the center of the channel is once again constant, and will remain constant for all later times.

When comparing the different channel sizes in Fig. 4, a number of observations can be made. First, an increase in channel size results in an increase in the duration of Period 1. This is a result of it taking longer for the EOF to diffuse all the way to the center of the channel. Second, an increase in the channel size results in a decrease in the duration of Period 3. The microchannels with larger dimensions take less time for a pressure gradient to build up and start affecting the steady state EOF. Third, as the channel keeps increasing in size, especially for larger aspect ratio channels, the pressure effects can arrive so early as to preclude the development of a Period 3. Fig. 4.b demonstrates that the pressure affects within the 800 x 8000 μm channel began to impact the fluid velocity within Period 2. This prevents the fluid flow in the largest channels from reaching Period 3 where steady state EOF occurs. Fourth, when comparing Period 2 across all the channel sizes and aspect ratios, it is shown that the flow acceleration is independent of the channel dimensions. It is only affected by a change in electric field or electrolyte and zeta potential, not shown here for brevity. Last, when comparing square channels with rectangular channels with the same height dimension but larger widths, the rectangular channels show earlier transition into Periods 4 and 5 as a result of a faster pressure build up.

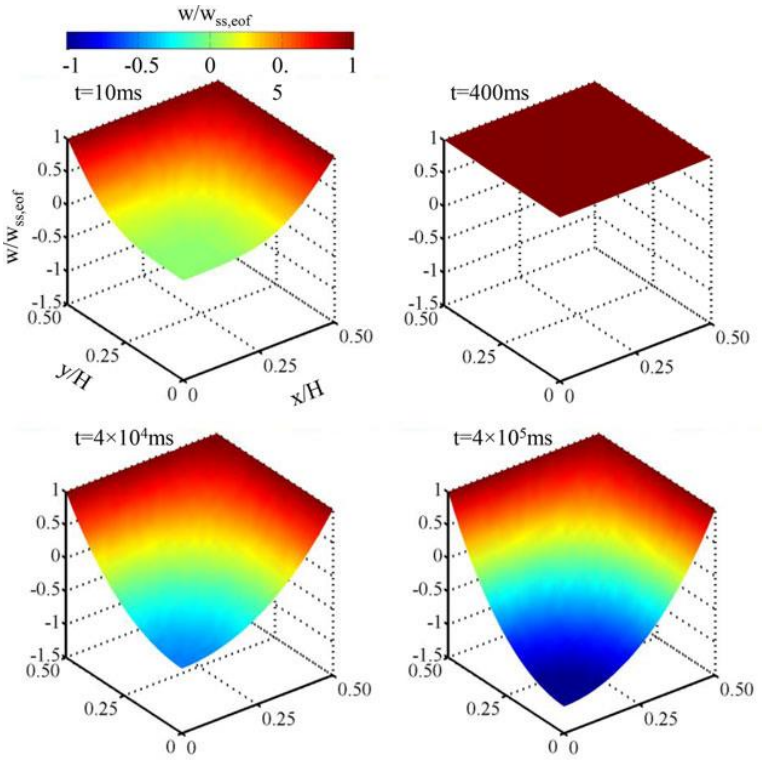

Figure 5. Temporal evolution of the velocity profile in the 800 μm **square glass channel under an applied electric field of 100 V/cm.**

To better understand the fluid flow behavior throughout the five periods described previously, a 2D representation of the full transient solution of the flow velocity is shown in Figs. 5 and 6. Results are presented as contour surface plots of the fluid velocity in the microchannel cross-section at four different times of interest (due to symmetry, only a quarter of the cross-section is shown). The time series in Fig. 5 shows the solution for an 800 μm square channel for an applied electric field of 100 V/cm. At time $t = 0$, the velocity at the walls is the slip velocity, while the velocity at the rest of the cross section is zero. Within the first 10 ms, the electroosmotic velocity propagates to the center of the channel, resulting in a parabolic velocity profile that can be considered at the limit between regions 1 and 2 in this transient process (see also Fig. 4a). Between Periods 2 and 3 the fluid is accelerated till it reaches the electroosmotic steady state velocity ($w_{ss,eof} = 405 \mu m / s$), which

happens at 400ms and determines the end of Period 2 and the beginning of Period 3. At this time, the velocity profile is nearly flat and the flow is moving at the slip velocity. For this geometry, Period 3 only lasts for a short duration (as previously discussed in Fig. 4) and Period 4 begins shortly afterwards at t > 400-500 ms, immediately after the velocity starts dropping due to the adverse pressure gradient. Period 4 extends up to t ~ 4×10^5 ms as shown in Fig. 4. A typical velocity profile during Period 4 is presented in Fig. 5 for t=4×10^4 ms, showing that at the center of the channel the normalized velocity is nearly -1. This indicates that the flow moves in one direction along the walls due to the electroosmotic effect, while simultaneously moving in the opposite direction along the center of the channel due to the buildup of the adverse pressure gradient. Period 5 is presented in Fig. 5 for t = 4×10^5 ms showing the final 2D steady state velocity profile for this flow which results in a net zero flow rate across the channel. This velocity profile will remain the same for any time t > 4×10^5ms.

To study the effect of channel aspect ratio on the transient velocity profile, contour plots of the fluid flow velocity in a rectangular channel (800×8000μm, AR=10) are shown in Fig. 6 for four different times. These can be compared to the square channel (800×800μm, AR=1) results in Fig. 5. The velocity has the same parabolic profile for both channel types during Period 1 and most of Period 2. For the rectangular channel the fluid flow is accelerated but does not reach the steady electroosmotic velocity everywhere. A maximum velocity in the center of the channel of $w_{max} = 321\mu m/s < w_{ss,eof}$ is reached, and the peak in velocity determines the end of Period 2. For this large microchannel geometry, Period 3 does not exist and Periods 2 and 4 overlap due to the speed at which the pressure gradient grows, even extending into the early startup periods of the electroosmotic flow.

Therefore, both the electrokinetically induced acceleration and the developing pressure induced velocity are important during Periods 2 and 4. The flow is then further decelerated until it reaches zero flow rate at the onset of Period 5.

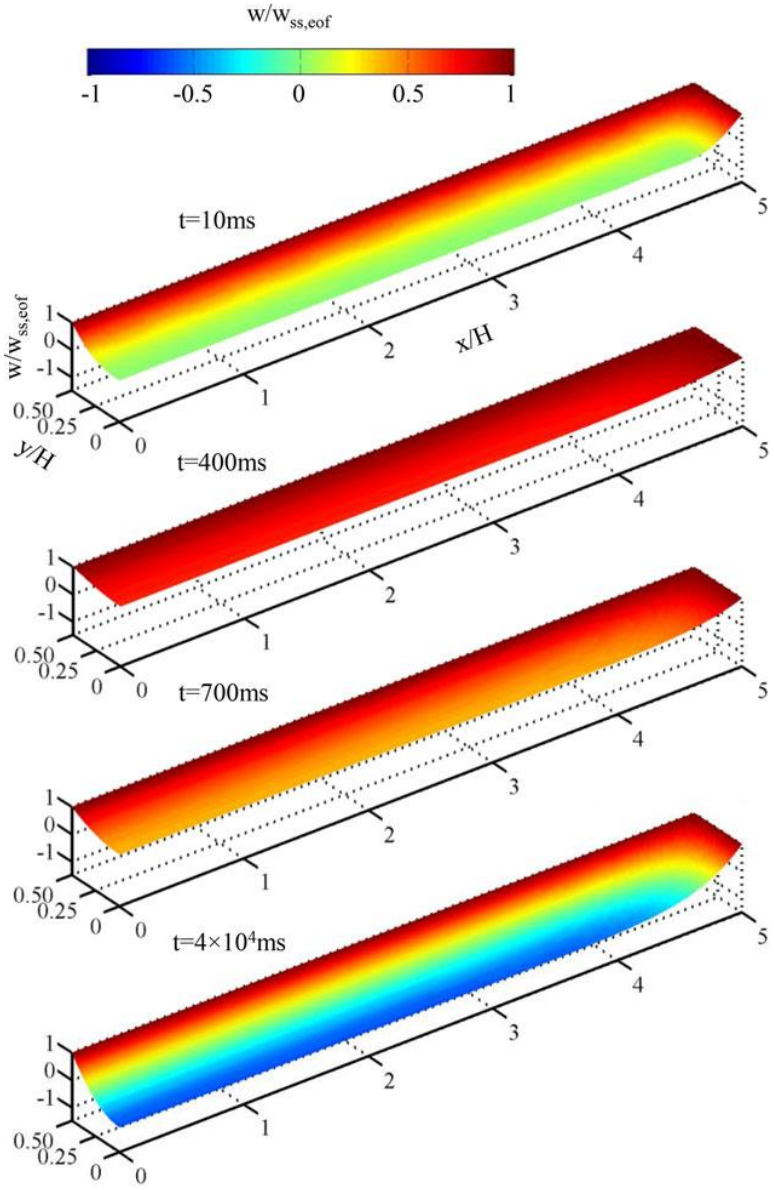

Figure 6. Temporal evolution of the velocity profile in the 800 x 8000 μm rectangular glass channel under an applied electric field of 100 V/cm.

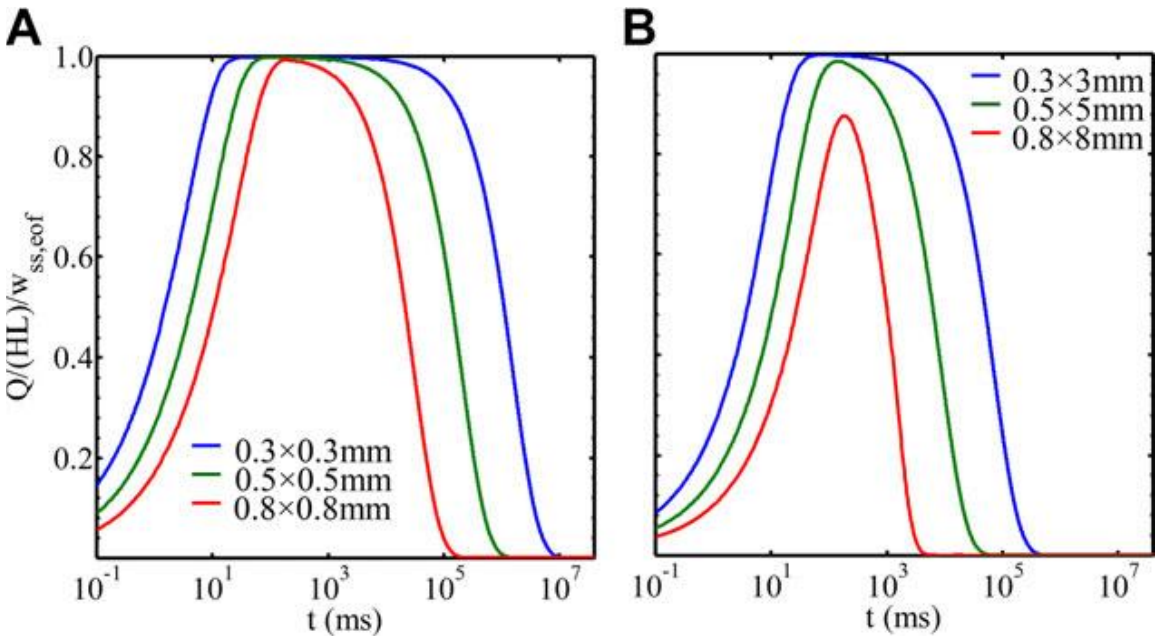

Figure 7. Temporal evolution of the analytical flow rate under an applied electric field of 100 V/cm for both (A) square and (B) rectangular glass channels.

Knowledge of the full 2D velocity profile allows a direct calculation of the transient volumetric flow rate $Q(t)$ by integrating this velocity profile (Eq. (18)). The evolution of the flow rate per unit area for the six different geometries is shown in Fig. 7. The five different developmental periods can also be identified within the transient volumetric flow rate in all the microchannels. In Period 1, as the EOF diffuses towards the center of the channel, the flow rate is very small. This is followed by Period 2, where $Q(t)$ quickly increases as the EOF fully develops. The volumetric flow rate reaches a quasi-steady maximum flow rate at the onset of Period 3. This period is defined by a near constant flow rate that expands up to $t = 1\times10^4$ ms for the 300 x 300 μm channel. For larger channels, Period 3 is significantly reduced (i.e.: $t = 1\times10^3$ ms for 500 x 500 μm), and in the limit (i.e.: $t\sim1\text{-}2\times10^2$ ms for 800 x 800 μm) the steady state EOF is barely reached before the developing adverse pressure gradient across the finite reservoirs begins to decrease the

flow rate. Period 4 is characterized by the growing adverse pressure gradient effect, which gradually decreases the flow rate until the average velocity across the channel's cross-section is zero. Period 5 starts when the volumetric flow rate has become zero across the channel, with the reservoir/channel system acting similarly to a closed cell.

To analyze the differences between channel sizes, Fig. 7a and 7b show the evolution of the flow rate for both square and rectangular channels respectively. The comparison shows that the onset of Period 2 is earlier for the smaller channels. This allows the smaller channels to achieve a fully established Period 3 earlier, and it gives rise to a maximum normalized flow rate 100-400 ms faster than seen within the larger channels considered. Furthermore, the maximum flow rate seen within the smaller channels remains constant for longer durations in Period 3. Next, the smaller microchannels have less volumetric flow rate, which in turn slows down the development of the adverse pressure gradient across the finite reservoirs. Finally, Period 5 is reached later for smaller channels compared to bigger channels since the deceleration rate is the same for all channel sizes. A similar behavior is observed within the rectangular channels as shown in Fig. 7b.

The impact of the channel's aspect ratio on the fluid's transient development is investigated by comparing Figs. 7a and 7b. The time constant signifying the start of Period 2 is nearly the same between the different aspect ratio channels. This follows as the time constant for the electrically induced wall slip velocity to diffuse into the center of the microchannel is a function only of the smallest channel cross-sectional dimension. However, the electroosmotic steady state (Period 3) is reached later for larger aspect ratios since more fluid needs to be accelerated. Alongside this, the end of Period 3 and the beginning of Period 4 is reached sooner for channels of higher aspect ratio due to the larger

volumetric flow rate, leading to a more quickly developing pressure gradient across the finite reservoirs. Together these effects cause Period 3 to be shorter in duration for larger aspect ratio channels.

The phenomena by which Period 4 can arrive much sooner in a larger aspect ratio channel is illustrated by the velocity development at the center of the 800×8000μm rectangular channel, shown in Fig. 7b. In this illustration, the pressure induced velocity becomes significant even before the electroosmotic flow has achieved its steady, fully developed condition. As such, Period 3 is never able to fully manifest itself in this channel's transient development. Instead an overlap of regions 2 and 4 is obtained for this channel geometry.

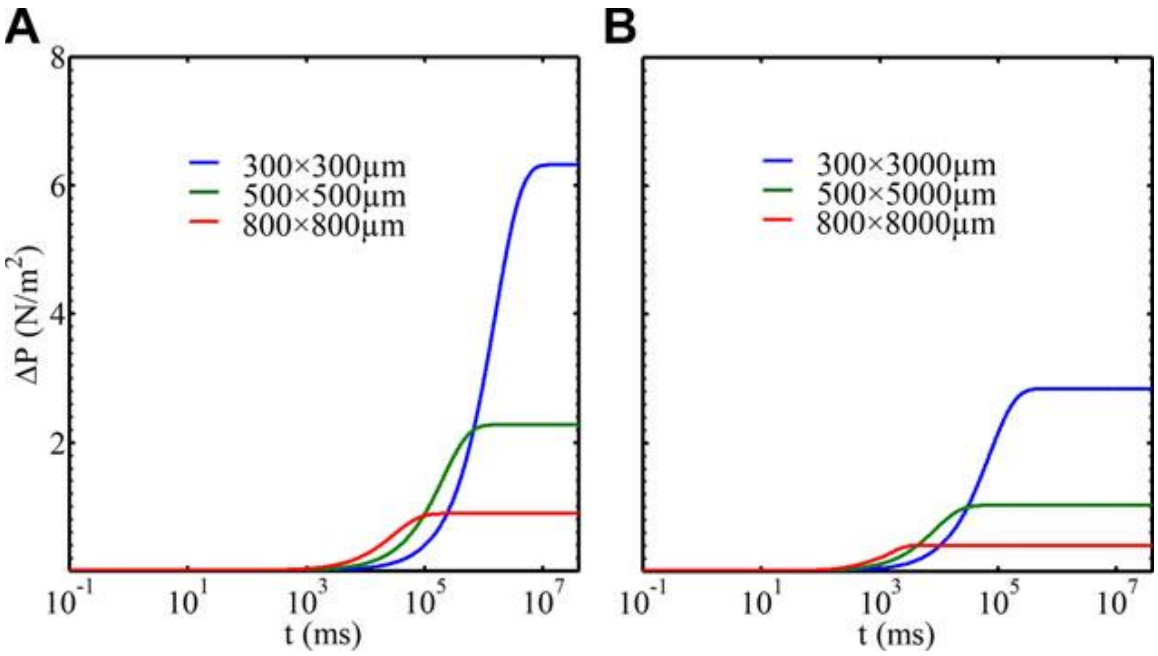

Figure 8. Temporal evolution of the analytical pressure differences across the channels under an applied electric field of 100 V/cm for both (A) square and (B) rectangular glass channels.

The nature of the electroosmotic flow, combined with the use of finite reservoirs, results in a time-varying pressure gradient that needs to be accurately determined in order to predict the velocity profile and the flow rate in a microchannel. The pressure difference between the channel's reservoirs is solved as a function of time using Eq. (10), and typical results are shown in Fig. 8 for the channels and geometries considered in Figs. 4 and 7. Three distinct phases are identified in the developing pressure difference between the finite reservoirs of a microchannel. In the first phase, the pressure difference remains small and is negligible within the flow development. In the second phase, the pressure gradient starts to increase ($t \sim 10^2 - 10^3$ ms), and continues to increase until it reaches a maximum pressure difference between the reservoirs. This is followed by a steady state third phase during which the pressure difference between the reservoirs is at a maximum and constant value.

The effect of channel size on the developing pressure gradient between the reservoirs is presented in Fig. 8a. It shows a sudden increase in pressure difference occurring earlier for channels of larger dimensions. This is the result of higher volumetric flow rates in larger channels inducing a more rapidly developing pressure gradient. This also means that the maximum pressure difference across the channel is reached in a shorter time in larger channels. However, the maximum pressure difference that can be achieved across a device's reservoirs is smaller for larger channels as the pressure is acting over a larger cross sectional area. A similar behavior is observed within the rectangular channels shown in Fig. 8b. The effect of the channel aspect ratio on the pressure differences induced across the channel is obtained by comparing Figs. 8a and 8b. Results show that the onset of phase 2 of the pressure development occurs earlier for larger aspect ratio channels since flow rate is considerably higher and the pressure builds up faster. In addition, the

maximum pressure difference between the reservoirs is reached earlier for larger aspect ratio channels. However, the maximum pressure that can be achieved across the channel is smaller for larger aspect ratios since the pressure acts in a larger channel cross-sectional area. This is expected since the adverse pressure induced flow rate per unit area given by Eq. (26) increases with aspect ratios for a fixed channel height, while the steady state electroosmotic flow rate per unit area is independent of the aspect ratio.

3.2 Experimental results

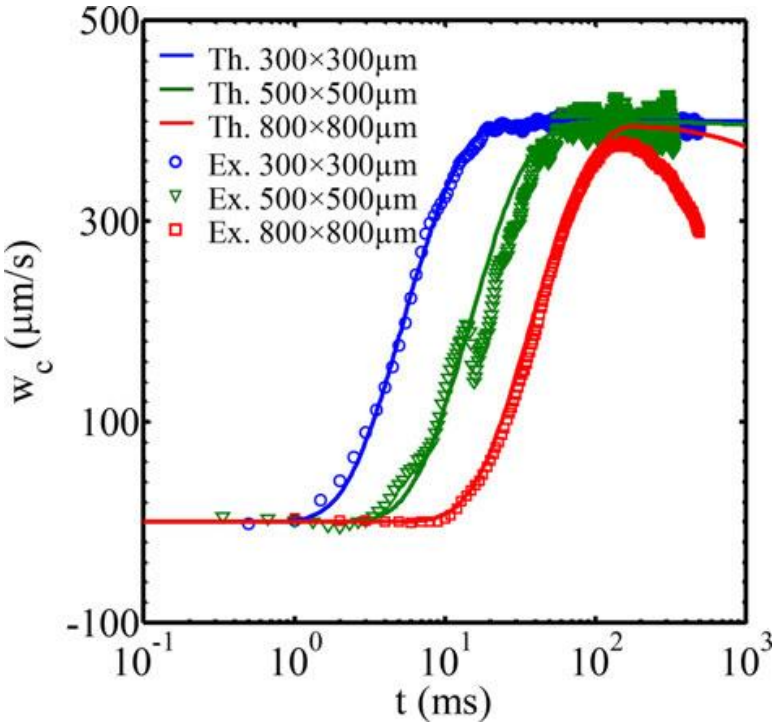

Figure 9. Temporal evolution of the velocity at the center of square glass channels under an applied electric field of 100 V/cm. Lines represent the theory and symbols represent the experimental data.

The analytical solution for the transient electroosmotic flow is validated experimentally from particle velocity measurements during the five periods previously identified. Experimental and analytical results showed good agreement for three different sized square channels, as shown in Fig. 9. These results show that the theory is able to capture the acceleration of the flow and predict the steady state electroosmotic velocity. During the measurements in Fig. 9, recording time was limited by the hardware to ~500ms, which covered only Periods 1, 2 and 3 for the geometries used. In Period 1, the measurements in the center of the channel show that electroosmotic slip velocity induced at the walls has not yet reached the center. Transition to Period 2 occurs when the fluid at the center of the

channel starts to accelerate from the induced electrical field. Period 3 in the transient development begins after the flow has reached EOF steady state. Onset of Period 4 occurs when the pressure gradient becomes significant and induces an adverse velocity in the channel. This is illustrated in Fig. 9 by the deceleration of the measured flow velocity for the 800 μm channel. For this same channel, the steady state electroosmotic velocity is not fully achieved and Period 3 is not able to fully develop. For the 300 and 500μm channels, the velocity decay associated with the start of Period 4 occurs beyond the experimental measurement range. For those two cases, the value of the pressure gradient and the time to reach zero volumetric flow rate can be estimated from the theory, as shown in Figs. 7 and 8.

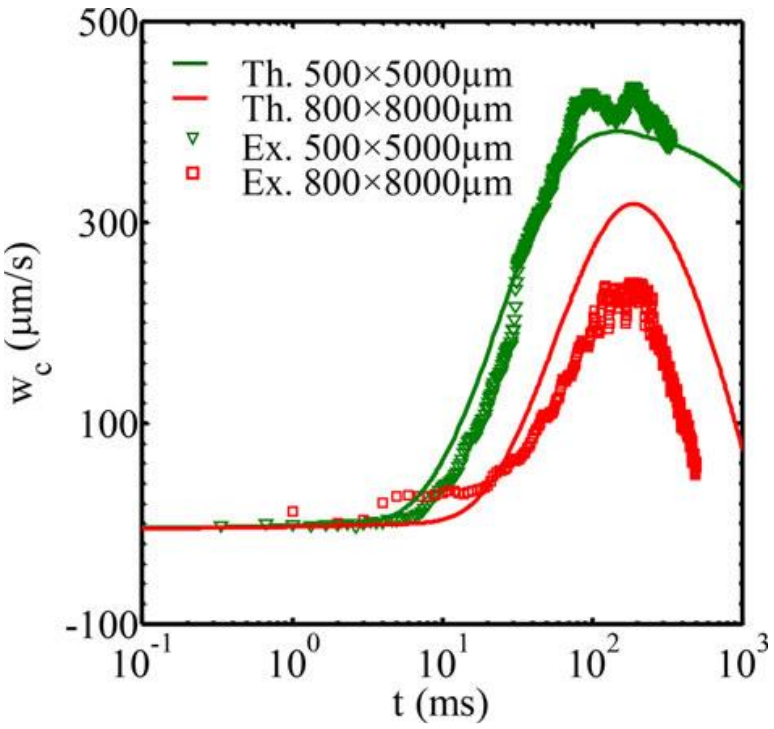

Figure 10. Temporal evolution of the velocity at the center of the rectangular glass channels under an applied electric field of 100 V/cm. Lines represent the theory and symbols represent experimental data.

To evaluate the effect of the channel aspect ratio on the transient velocity, measurements are performed on two channels with rectangular cross-sections, 500×5000μm and 800×8000 μm in size. Experimental and analytical results are presented in Fig. 10 for each channel tested. Similar behaviors are observed for both square and rectangular channels when comparing Figs. 9 and 10. Results from Period 1 and 2 show good agreement between theory and experiments. Period 3 is unable to be achieved in both geometries. Period 4 appears earlier during the experiments for the larger 800×8000μm channel. In this case, the fluid flow in the channel is affected very early on by the development of the adverse pressure gradient and the fluid in the channel is unable to reach more than 60% of the expected maximum electroosmotic velocity.

The experimental results agree qualitatively with those predicted by theory. However, there are deviations from the expected results, most markedly being the earlier than expected development of the pressure gradient induced velocity component in the 800×8000 μm channel. This difference is attributed to experimental error in the setup of the microdevice and inaccurate measurement of the channel's reservoirs. It is also possible that non-ideal conditions associated with the laboratory environment, or affects not captured in the theoretical model such as surface tension in the reservoirs, could have impacted the results.

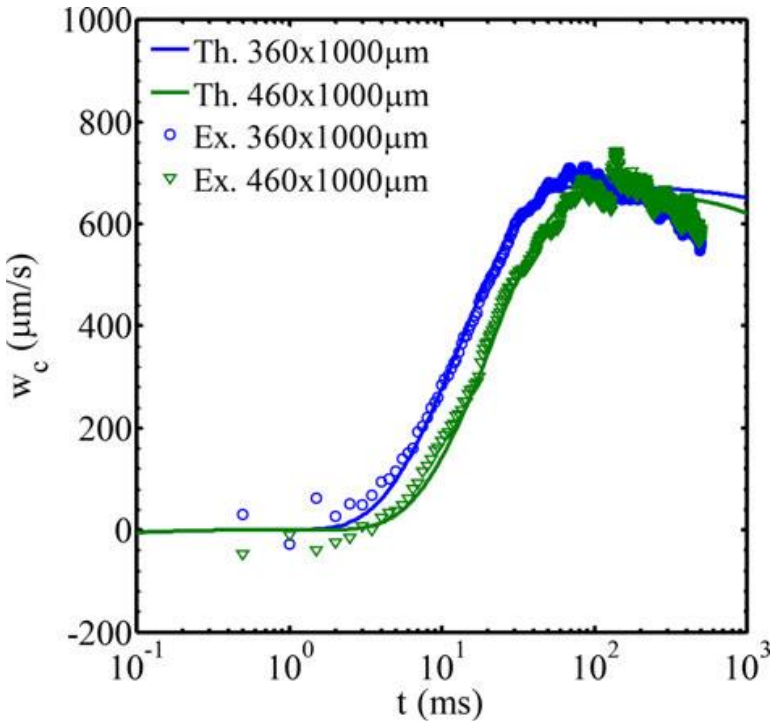

Figure 11. Temporal evolution of the velocity at the center of the rectangular PDMS channels under an applied electric field of 200 V/cm. Lines represent the theory and symbols represent the experimental data.

Channels with different wall surfaces are common in microfluidics, in particular PDMS channels with the bottom wall made out of quartz to facilitate microscope visualization. The proposed analytical model is able to handle channels comprised of different walls with different zeta potentials. To test this capability, measurements were performed on channels with three PDMS walls and the fourth wall made out of quartz glass. The results are compared to the analytical model in Fig. 11, showing excellent agreement during Periods 1, 2, 3 and 4. Due to the large aspect ratios of the channels and the stronger applied electric field (E = 200 V/cm), each channel maintained a large volumetric flow rate. As such, Period 3 was kept very short, with the onset of Period 4 occurring early (t ~100 ms) due to the rapid development of the adverse pressure gradient.

This analysis shows that the analytical model can handle asymmetric flows resulting from channels with different wall boundary conditions and zeta potentials.

4 Concluding remarks

An analytical and an experimental study of the transient startup electroosmotic flow in rectangular channels was presented in this work. The analytical solution is obtained from the two most general governing relations for electroosmotic flows, the Navier-Stokes equations and the Poisson-Boltzmann equation. The analytical solution allows the identification of five distinct periods within the transient flow in a microchannel. In Period 1, the electroosmotic flow, EOF, is initiated at the wall by an instantly applied electric field. Period 1 is characterized by the electrokinetically induced slip velocity diffusing from the walls but having not yet reached the center of the channel. In Period 2, the EOF has reached the center of the channel, and the fluid is accelerating towards a fully developed and steady state EOF profile throughout the cross-section of the channel. In Period 3, the flow has reached a quasi-steady state due to a constant and fully developed EOF. Period 4 occurs when the adverse pressure gradient induced velocity is large enough to significantly affect the channel's velocity profiled. Period 4 is characterized by a reversal of the velocity profile in the center of the channel, driving the volumetric flow rate in the channel towards zero. When the volumetric flow rate in the channel reaches zero, Period 5 is reached and the fluid has reached its final steady state profile. In this state the microchannel performs as if it were a closed cell system, with the fluid moving in one direction along the walls due to the electroosmotic effect while moving in the opposite direction along the center of the channel due to the pressure gradient.

Variants of the five periods are observed depending on the cross-sectional size and aspect ratio of the channel. An increase in channel size results in a lengthening of Period 1 but a decrease in the duration of Period 3. Period 2's duration was largely unaffected by

channel size. Also, when comparing the transient development of square channels with rectangular channels of the same height but larger width, the rectangular channels show earlier transitions into Periods 3, 4 and 5 as a result of a larger volumetric flow rate and corresponding pressure build up. For the largest channels tested, Period 3 did not develop as a distinct phase, as the pressure gradient was already significant compared to the EOF in Period 2.

The analytical solution for the 2D velocity profile allows the calculation of the transient volumetric flow rate $Q(t)$. Results show that the five periods proposed can also be identified during the time evolution for $Q(t)$ for the channel sizes and aspect ratios considered. For example, the flow rate remained constant in Period 3 for longer durations for the smaller channels considered, and the duration of Period 3 decreased as the channel size was increased. Similarly, Period 5 was reached later as the channels' cross-sectional dimensions became smaller. The effect of the time-varying pressure gradient on the velocity profile was also investigated, giving rise to three distinctive periods. In the first period, the pressure gradient remains small and has a negligible impact upon the flow development in the channel. In the second period, the pressure gradient starts to increase ($t \sim 10^2 - 10^3$ ms), continuing to rise until it reaches a maximum pressure difference across the channel. This is followed by a third period characterized by a constant and maximum pressure difference across the channel.

The analytical solution for the transient electroosmotic flow was validated using a TR-μPIV system. The electroosmotic velocity is calculated by subtracting the tracer particles' electrophoretic velocity from the PIV measured velocity. As predicted by the analytical model, the measurements also demonstrated the five developmental periods

previously identified. Experimental and analytical results showed good agreement for all periods compared. The measurements captured the acceleration of the flow during Period 2 and predicted the steady state electroosmotic velocity in Period 3. Measurements also showed that during Period 4 the pressure gradient becomes important and induces an adverse velocity that decelerates the flow. Results showed that Period 3 was missing from the larger microchannels, as predicted by the theory. This is due to the rapid development of the adverse pressure gradient induced velocity, which prevented the fluid from reaching the typical quasi-steady state EOF profile in Period 3. Lastly, channels with three PDMS walls and a fourth wall made out of quartz were also tested and compared to the theory to demonstrate the capabilities of the analytical model to handle channels with different wall zeta potentials. Experimental results showed excellent agreement with the theoretical model, with accurate predictions being made for the time durations and fluid flow velocities during Periods 1, 2, 3, and 4 of each channel's development. This analysis shows that the analytical model can handle asymmetric flows resulting from channels with different wall boundary conditions and zeta potentials.

5 Appendix A

The solution to Eq. (13) is found by using the method of separation of variables. Since Eq.(13) is linear, the solution can be separated into the transient and steady state portions as:

$$w(x,y,t) = w_{tran}(x,y,t) + w_{SS}(x,y) \tag{27}$$

where the subscript "SS" stands for steady state. By substituting Eq. (27) into Eq. (13) and rearranging terms we get:

$$\frac{\partial w_{tran}}{\partial t} - \nu\left(\frac{\partial^2 w_{tran}}{\partial x^2} + \frac{\partial^2 w_{tran}}{\partial y^2}\right) = -\frac{1}{\rho}\frac{dp}{dz} + \nu\left(\frac{\partial^2 w_{SS}}{\partial x^2} + \frac{\partial^2 w_{SS}}{\partial y^2}\right) . \tag{28}$$

The steady state fluid velocity must satisfy:

$$0 = -\frac{dp}{dz} + \mu\left(\frac{\partial^2 w_{SS}}{\partial x^2} + \frac{\partial^2 w_{SS}}{\partial y^2}\right) . \tag{29}$$

Since the governing equation for the steady state fluid velocity (29) is also linear, the velocity can be further separated into the electrokinetic and pressure gradient terms:

$$w_{SS} = w_{SS}^{EK} + w_{SS}^{pressure} . \tag{30}$$

Substituting Eq. (30) into Eq. (29) yields:

$$0 = -\frac{dp}{dz} + \mu\left(\frac{\partial^2\left(w_{SS}^{pressure} + w_{SS}^{EK}\right)}{\partial x^2} + \frac{\partial^2\left(w_{SS}^{pressure} + w_{SS}^{EK}\right)}{\partial y^2}\right) . \tag{31}$$

Simplifying Eq. (31) yields:

$$0 = -\frac{dp}{dz} + \mu\nabla^2 w_{SS}^{pressure} + \mu\nabla^2 w_{SS}^{EK} \tag{32}$$

The portion of the solution associated with the fluid being electrokinetically driven must satisfy the following condition:

$$\mu\nabla^2 w_{SS}^{EK} = 0 \tag{33}$$

As given in Eqs. (16-17), the electrokinetically driven boundary conditions are:

$$w_{SS}^{EK}\left(x,-\frac{H}{2},t\right)=-\frac{\varepsilon\zeta_2}{\mu}E \tag{34}$$

$$w_{SS}^{EK}\left(-\frac{L}{2},y,t\right)=w_{SS}^{EK}\left(\frac{L}{2},y,t\right)=w_{SS}^{EK}\left(x,\frac{H}{2},t\right)=-\frac{\varepsilon\zeta_1}{\mu}E \tag{35}$$

The solution to this governing equation is given by [6]:

$$w_{SS}^{EK}(x,y)=-\frac{\varepsilon E\zeta_1}{\mu}+\frac{\varepsilon E}{\mu}(\zeta_1-\zeta_2)\frac{2}{\pi}\sum_{k=1}^{\infty}\frac{1+(-1)^{k+1}}{k}\sin\left(\frac{k\pi\left(x+\frac{L}{2}\right)}{L}\right)\frac{\sinh\left(\frac{k\pi\left(-y+\frac{H}{2}\right)}{L}\right)}{\sinh\left(\frac{k\pi H}{L}\right)} \tag{36}$$

Returning to Eq. (32), a solution is sought for the pressure driven portion of the steady state velocity field:

$$0=-\frac{dp}{dz}+\mu\nabla^2 w_{SS}^{pressure} \tag{37}$$

The boundary conditions for Eq. (37) are:

$$w_{SS}^{pressure}\left(-\frac{L}{2},y,t\right)=w_{SS}^{pressure}\left(\frac{L}{2},y,t\right)=w_{SS}^{pressure}\left(x,-\frac{H}{2},t\right)=w_{SS}^{pressure}\left(x,\frac{H}{2},t\right)=0 \tag{38}$$

The solution to this governing equation and the associated conditions is given by [6]:

$$w_{SS}^{pressure}=\frac{-2H^2}{\pi^3\mu}\frac{dp}{dz}\sum_{j=1}^{\infty}\frac{1+(-1)^{j+1}}{j^3}\left[1-\frac{\cosh\left(\frac{j\pi x}{H}\right)}{\cosh\left(\frac{j\pi L}{2H}\right)}\right]\sin\left(\frac{j\pi\left(y+\frac{H}{2}\right)}{H}\right) \tag{39}$$

From Eq. (28), the transient equation must satisfy:

$$\frac{\partial w_{tran}}{\partial t}-\nu\nabla^2 w_{tran}=0\ . \tag{40}$$

The boundary conditions for the transient solution are given by:

$$w_{tran}\left(-\frac{L}{2},y,t\right)=w_{tran}\left(\frac{L}{2},y,t\right)=w_{tran}\left(x,-\frac{H}{2},t\right)=w_{tran}\left(x,\frac{H}{2},t\right)=0\,. \tag{41}$$

The transient solution's initial condition is given by:

$$w(x,y,0)_{tran}=w(x,y,0)-w_{SS}(x,y) \tag{42}$$

This yields:

$$w(x,y,0)_{tran}=-w_{SS}(x,y)\,. \tag{43}$$

The solution to Eq. (40) is found by the method of separation of variables:

$$w_{tran}(x,y,t)=X(x)Y(y)T(t)\ . \tag{44}$$

Substituting Eq. (44) into Eq. (40) gives the following relation:

$$\frac{1}{\nu}\frac{T'}{T}=\frac{X''}{X}+\frac{Y''}{Y}=-\kappa^2\ . \tag{45}$$

Isolating *T(t)* from Eq. (45) yields:

$$T(t)=Ae^{-\nu\kappa^2 t} \tag{46}$$

Revisiting Eq. (45) leaves:

$$\frac{X''}{X}+\frac{Y''}{Y}=-\kappa^2 \tag{47}$$

Isolating *X(x)* from Eq. (47) gives:

$$X(x)=E_n\cos\left(\alpha\left(x+\frac{L}{2}\right)\right)+F_n\sin\left(\alpha\left(x+\frac{L}{2}\right)\right) \tag{48}$$

The boundary condition at the left wall from Eq. (41) can now be applied as:

$$X\left(-\frac{L}{2}\right)=E_n\cos(0)+F_n\sin(0)=0 \tag{49}$$

$$E_n=0 \tag{50}$$

Similarly, we can also solve for $Y(y)$ to obtain:

$$Y(y) = G_m \cos\left(\sqrt{\kappa^2 - \alpha^2}\left(y + \frac{H}{2}\right)\right) + H_m \sin\left(\sqrt{\kappa^2 - \alpha^2}\left(y + \frac{H}{2}\right)\right) . \tag{51}$$

The boundary condition at the bottom wall from Eq. (41) can now be applied as:

$$Y\left(-\frac{H}{2}\right) = G_m \cos(0) + H_m \sin(0) = 0 \tag{52}$$

$$G_m = 0 \tag{53}$$

Next, applying the boundary condition at the right wall and the top of the channel from Eq. (41) yields two additional relations:

$$X\left(\frac{L}{2}\right) = F_n \sin(\alpha L) = 0 \tag{54}$$

$$Y\left(\frac{H}{2}\right) = H_m \sin\left(\sqrt{\kappa^2 - \alpha^2}\right) = 0 \tag{55}$$

Eqs. (54-55) lead to the following relations for α and κ:

$$\alpha^2 = \frac{n^2\pi^2}{L^2} \tag{56}$$

$$\kappa^2 = \pi^2\left(\frac{n^2}{L^2} + \frac{m^2}{H^2}\right) \tag{57}$$

Substituting Eqs. (56) and (57) into Eqs. (46), (48) and (51) and combining terms, the total transient solution from Eq. (44), can now be expressed as:

$$w_{tran}(x,y,t) = \sum_{n=1}^{\infty}\sum_{m=1}^{\infty} C_{m,n} \sin\left(\frac{n\pi\left(x + \frac{L}{2}\right)}{L}\right) \sin\left(\frac{m\pi\left(y + \frac{H}{2}\right)}{H}\right) e^{-\nu\pi^2\left(\frac{n^2}{L^2} + \frac{m^2}{H^2}\right)t} \tag{58}$$

The next step is to apply the initial condition from Eq. (43), which results in:

$$w_{tran}\left(x,y,0\right)=\sum_{n=1}^{\infty}\sum_{m=1}^{\infty}C_{m,n}\sin\left(\frac{n\pi\left(x+\frac{L}{2}\right)}{L}\right)\sin\left(\frac{m\pi\left(y+\frac{H}{2}\right)}{H}\right)=-w_{SS} \tag{59}$$

The terms $C_{m,n}$ in Eq. (59) are found via the integral:

$$C_{m,n}=\frac{4}{HL}\int_{-H/2}^{H/2}\int_{-L/2}^{L/2}(-w_{SS})\sin\left(\frac{n\pi\left(x+\frac{L}{2}\right)}{L}\right)\sin\left(\frac{m\pi\left(y+\frac{H}{2}\right)}{H}\right)dxdy \tag{60}$$

where, $w_{SS}=w_{SS}^{EK}+w_{SS}^{pressure}$.

Finally, the equation for the velocity field in a fully developed channel with an arbitrary pressure gradient, electric field, and zeta potentials at each of its walls is:

$$
\begin{aligned}
w(x,y,t) = & -\frac{\varepsilon E \zeta_1}{\mu} \\
& + \frac{\varepsilon E}{\mu}\left(\zeta_1 - \zeta_2\right)\frac{2}{\pi}\sum_{k=1}^{\infty}\frac{1+\left(-1\right)^{k+1}}{k}\sin\left(\frac{k\pi\left(x+\frac{L}{2}\right)}{L}\right)\frac{\sinh\left(\frac{k\pi\left(-y+\frac{H}{2}\right)}{L}\right)}{\sinh\left(\frac{k\pi H}{L}\right)} \\
& - \frac{2H^2}{\pi^3\mu}\frac{dp}{dz}\sum_{j=1}^{\infty}\frac{1+\left(-1\right)^{j+1}}{j^3}\left[1-\frac{\cosh\left(\frac{j\pi x}{H}\right)}{\cosh\left(\frac{j\pi L}{2H}\right)}\right]\sin\left(\frac{j\pi\left(y+\frac{H}{2}\right)}{H}\right) \\
& + \sum_{n=1}^{\infty}\sum_{m=1}^{\infty}\left\{\left[\frac{4\varepsilon E\zeta_1}{mn\mu\pi^2}\left(1+\left(-1\right)^{n+1}\right)\left(1+\left(-1\right)^{m+1}\right)\right.\right. \\
& \quad - \frac{4\varepsilon E\left(\zeta_1-\zeta_2\right)}{H^2\mu}\frac{m}{n}\left[\frac{1+\left(-1\right)^{n+1}}{\frac{n^2\pi^2}{L^2}+\frac{m^2\pi^2}{H^2}}\right] \\
& \quad \left.\left. + \frac{4H^2}{\pi^4\mu}\frac{dp}{dz}\frac{\left(1+\left(-1\right)^{m+1}\right)}{m^3}\left[1-\frac{\frac{n^2\pi^2}{L^2}}{\left(\frac{m^2\pi^2}{H^2}+\frac{n^2\pi^2}{L^2}\right)}\right]\frac{\left(1+\left(-1\right)^{n+1}\right)}{n}\right] \right. \\
& \quad \left. \times\sin\left(\frac{n\pi\left(x+\frac{L}{2}\right)}{L}\right)\sin\left(\frac{m\pi\left(y+\frac{H}{2}\right)}{H}\right)e^{-\nu\pi^2\left(\frac{n^2}{L^2}+\frac{m^2}{H^2}\right)t}\right\}
\end{aligned}
\tag{61}
$$

6 References

[1] R. J. Hunter, “Zeta potential in colloid science: principles and applications,” 1981.

[2] J. H. Masliyah and S. Bhattacharjee, *Electrokinetic and colloid transport phenomena*. John Wiley & Sons, 2006.

[3] C. Yang and D. Li, “Electrokinetic effects on pressure-driven liquid flows in rectangular microchannels,” *J. Colloid Interface Sci.*, vol. 194, no. 1, pp. 95–107, 1997.

[4] C. Yang and D. Li, “Analysis of electrokinetic effects on the liquid flow in rectangular microchannels,” *Colloids Surf. Physicochem. Eng. Asp.*, vol. 143, no. 2, pp. 339–353, 1998.

[5] C. D. Meinhart, S. T. Wereley, and J. G. Santiago, “PIV measurements of a microchannel flow,” *Exp. Fluids*, vol. 27, no. 5, pp. 414–419, 1999.

[6] S. Devasenathipathy, J. G. Santiago, and K. Takehara, “Particle Tracking Techniques for Electrokinetic Microchannel Flows,” *Anal. Chem.*, vol. 74, no. 15, pp. 3704–3713, Aug. 2002.

[7] D. Yan, C. Yang, N.-T. Nguyen, and X. Huang, “Electrokinetic flow in microchannels with finite reservoir size effects,” in *Journal of Physics: Conference Series*, 2006, vol. 34, p. 385.

[8] D. Yan, C. Yang, N.-T. Nguyen, and X. Huang, “A method for simultaneously determining the zeta potentials of the channel surface and the tracer particles using microparticle image velocimetry technique,” *Electrophoresis*, vol. 27, no. 3, pp. 620–627, 2006.

[9] D. G. Yan, C. Yang, and X. Y. Huang, “Effect of finite reservoir size on electroosmotic flow in microchannels,” *Microfluid. Nanofluidics*, vol. 3, no. 3, pp. 333–340, Apr. 2007.

[10] C.-Y. Wang, Y.-H. Liu, and C. C. Chang, “Analytical solution of electro-osmotic flow in a semicircular microchannel,” *Phys. Fluids 1994-Present*, vol. 20, no. 6, p. 063105, 2008.

[11] W. Lei, W. Jiankang, and C. Bo, “Analytic Solution of Liquid Flow in Rectangular PDMS-GLASS Microchannel with Wall Slip and Electro-Viscous Effects,” *Appl. Math. Sci.*, vol. 3, no. 44, pp. 2195–2214, 2009.

[12] C. D. Meinhart, S. T. Wereley, and M. H. B. Gray, “Depth effects in volume illuminated particle image velocimetry,” *Meas Sci Technol*, vol. 11, pp. 809–814, 2000.

[13] X. Yang and J. Yan, “Principles for the Measurement and Image Processing Using PIV [J],” *Sichuan Univ. Sci. Technol.*, vol. 1, p. 005, 2005.

[14] Marcos, C. Yang, K. T. Ooi, T. N. Wong, and J. H. Masliyah, “Frequency-dependent laminar electroosmotic flow in a closed-end rectangular microchannel,” *J. Colloid Interface Sci.*, vol. 275, no. 2, pp. 679–698, Jul. 2004.

[15] K. Shinohara, Y. Sugii, A. Aota, A. Hibara, M. Tokeshi, T. Kitamori, and K. Okamoto, “High-speed micro-PIV measurements of transient flow in microfluidic devices,” *Meas. Sci. Technol.*, vol. 15, no. 10, p. 1965, 2004.

[16] D. Yan, N.-T. Nguyen, C. Yang, and X. Huang, “Visualizing the transient electroosmotic flow and measuring the zeta potential of microchannels with a micro-PIV technique,” *J. Chem. Phys.*, vol. 124, no. 2, p. 021103, 2006.

[17] D. Yan, C. Yang, N.-T. Nguyen, and X. Huang, “Diagnosis of transient electrokinetic flow in microfluidic channels,” *Phys. Fluids*, vol. 19, no. 1, p. 017114, 2007.
[18] C. C. Chang and C. Y. Wang, “Starting electroosmotic flow in an annulus and in a rectangular channel,” *Electrophoresis*, vol. 29, no. 14, pp. 2970–2979, 2008.
[19] C. C. Chang and C.-Y. Wang, “Electro-osmotic flow in a sector microchannel,” *Phys. Fluids 1994-Present*, vol. 21, no. 4, p. 042002, 2009.
[20] C. Kuang, F. Yang, W. Zhao, and G. Wang, “Study of the rise time in electroosmotic flow within a microcapillary,” *Anal. Chem.*, vol. 81, no. 16, pp. 6590–6595, 2009.
[21] C. Kuang, R. Qiao, and G. Wang, “Ultrafast measurement of transient electroosmotic flow in microfluidics,” *Microfluid. Nanofluidics*, vol. 11, no. 3, pp. 353–358, 2011.
[22] M. Sureda, A. Miller, and F. J. Diez, “In situ particle zeta potential evaluation in electroosmotic flows from time-resolved microPIV measurements,” *Electrophoresis*, vol. 33, no. 17, pp. 2759–2768, 2012.
[23] R. F. Probstein, “Physicochemical Hydrodynamics: An Introduction Wiely,” *N. Y.*, 1994.
[24] M. Minor, A. J. Van der Linde, H. P. Van Leeuwen, and J. Lyklema, “Dynamic aspects of electrophoresis and electroosmosis: a new fast method for measuring particle mobilities,” *J. Colloid Interface Sci.*, vol. 189, no. 2, pp. 370–375, 1997.

7 Previous Publications

Miller, A., Villegas, A., Diez, F., (2015). “Characterization of the startup transient electrokinetic flow in rectangular channels of arbitrary dimensions, zeta potential distributions, and time-varying pressure gradient.” Electrophoresis, 36(5): 692-702.

Sureda, M., Miller, A., Diez, F., (2013). “In situ particle zeta potential evaluation in electroosmotic flows from time-resolved microPIV measurements.” Electrophoresis, 33(17): 2759-2768.